

Absence of quasi-classical coherence in mean-field dynamics of bosons in a kinetically frustrated regime

Akos Rapp

Institut für Theoretische Physik, Leibniz Universität, 30167 Hannover, Germany

(Dated: May 22, 2022)

We study numerically the dynamics of bosons on a triangular lattice after quenching both the on-site interactions and the external trapping potential to negative values. In a similar situation on the square lattice, the dynamics can be understood in terms of an effectively reversed Hamiltonian. On the triangular lattice, however, the kinetic part of the reversed Hamiltonian is frustrated and whether coherence can develop is an open question. The strength of the frustration can be changed by tuning the ratio of the hopping rates along different directions. We calculate time-of-flight images at different times after the quench for different values of the hopping anisotropy. We observe peaks at the maxima of the original non-interacting dispersion relation both in the isotropic case and also in the rhombic limit of high hopping anisotropy. For an intermediate value, however, no coherence develops up to the longest simulation times. These results imply that experiments along similar lines could study unconventional superfluidity of bosons and aspects of the conjectured spin-liquid behavior in the hard-core limit.

PACS numbers: 03.75.Nt, 67.85.-d,

I. INTRODUCTION

A broadly observed fact is that most physical systems undergo transitions to phases of matter which display some kind of order as the system is cooled down. In geometrically frustrated systems, however, such ordering may not be possible down to the lowest temperatures since the spatial arrangement is incompatible with certain order types. For classical Ising spins on the triangular lattice with antiferromagnetic coupling, this problem was first discussed by Wannier [1], who found finite ground state entropy, a consequence of a highly degenerate ground state. In three dimensions, frustration plays an important role in spin ice materials, which display magnetic monopoles [2], the microscopic version of the hypothetical cosmic counterpart proposed in the famous paper by Dirac [3]. Strong quantum fluctuations present for lower spin lengths can give rise to elusive spin liquid phases [4].

The identification of spin liquids in solid state systems is very challenging, on one hand, due to the featureless nature of the spin liquid phase, but also because of the interplay of additional degrees of freedom, phonons, disorder, etc. In contrast, ultracold atoms in optical lattices (see the review Ref. [5]) present exceptionally clean systems where microscopic parameters can be tuned experimentally in a broad range with great control. In addition, the relatively large typical spatial and time scales allow tracking physical processes more easily. Ultracold atoms in optical lattices are therefore ideal quantum simulators for many-body systems.

The realization of geometric frustration is not straightforward in optical lattices. One reason behind this is that the nearest-neighbor hopping amplitude J between lattice sites in the lowest Bloch band has a definite sign, usually defined with the convention $J > 0$. This is implied physically by the fact that the lowest energy usually

implies zero momentum and mathematically by the solution of the Mathieu equation describing the one-body problem in the one-dimensional standing wave optical lattice potential. Simple square or cubic lattices built from this potential naturally share this property, moreover, the non-interacting next-nearest-neighbor hopping is exactly zero due to the separability of the one-body problem.

The hopping amplitude in higher Bloch bands can have opposite signs, but such systems are not especially suitable for quantum simulations. One issue is the high instability with respect to decay to other bands, which is not easily circumvented [6, 7].

Frustrated antiferromagnetic Heisenberg models emerge naturally at low energies in Mott insulators of fermions in triangular lattices. However, the Heisenberg exchange energy is somewhat lower than the current typical temperatures in fermionic clouds and therefore antiferromagnetic long-range order has not yet been established even on bipartite lattices [8].

A very successful idea to effectively change the sign of the hopping amplitude $J \rightarrow J_{\text{eff}}$ is based on a periodic modulation of the optical lattice [9]. This idea lead to a proposal for bosons on the triangular lattice with an elliptical lattice shaking [10], which allows for a continuous tuning of the effective hopping anisotropically. Such bosons can be mapped to XY spin models in two limits of the interaction strength. For weak interactions and sufficiently high boson filling, each site can be described as an individual “superfluid” droplet with a well-defined phase and the bosonic Hamiltonian can be mapped to a *classical* XY-model. In the other limit, at half filling and infinitely strong repulsion, the Hamiltonian can be mapped to a *quantum* XY-model. Both of these models are frustrated with antiferromagnetic couplings, given by a negative effective hopping, $J_{\text{eff}} < 0$. In the case of isotropic nearest-neighbor spin couplings, it is

believed that both ground states exhibit 120° spiral long-range magnetic order [11, 12] (U(1) rotational symmetry breaking), with a non-zero chirality (Z_2 symmetry breaking). As the anisotropy of the couplings is increased, the chirality decreases and vanishes. In the classical model this happens at the so-called rhombic transition point, beyond which only the U(1) spin symmetry is broken. Most interestingly, it was proposed that in the hardcore limit, instead of a single phase transition, a gapped spin-liquid phase emerges between two quasi-classically ordered phases [12, 13]. The conjectured phase diagram for the bosons is displayed in Ref. [10]. While the lattice shaking technique succeeded experimentally in simulating frustrated classical magnetism [14, 15], no signature of the quantum magnetism has been reported so far.

An alternative route to reversed hopping is employing negative absolute temperatures, $T < 0$. Negative absolute temperatures can be reached in closed systems with Hamiltonians with an upper bound [16]. With ultracold atoms in optical lattices, such a Hamiltonian H can be engineered basically by switching the sign of the external harmonic trapping potential $V_0 > 0 \rightarrow V_0 < 0$ [17–22]. Energy conservation restricts the dynamics and the atomic cloud cannot explode as long as the kinetic energy is bounded. This latter condition is provided by a sufficiently deep optical lattice. In equilibrium at $T < 0$, the partition function of the system is equivalent to the partition function of a system at an effective temperature $|T|$ governed by the reversed Hamiltonian $-H$. In Ref. [19] it was discussed that this mapping can be used to realize Hamiltonians that have couplings with signs that are hard to reach experimentally. In this work we apply this idea to bosons on the triangular lattice, which, at negative T , have “frustrated” kinetic energy.

For concreteness, we consider bosons described by the Bose-Hubbard model

$$H = - \sum_{\langle ij \rangle} J_{ij} b_i^\dagger b_j + \frac{U}{2} \sum_j \hat{n}_j (\hat{n}_j - 1) + \sum_j (V_0 \mathbf{r}_j^2 - \mu_0) \hat{n}_j. \quad (1)$$

Here $J_{ij} > 0$ describes anisotropic nearest-neighbor hopping between sites i and j on an equiangular triangular lattice [c.f. Fig. 1], U is the on-site interaction strength, V_0 gives the strength of the external harmonic potential, and the central chemical potential μ_0 sets the total number of particles.

Numerically robust methods [exact diagonalization (ED), projected entangled pair states (PEPS) [23] or quantum Monte Carlo (QMC) [24]] are all very challenging to describe the Bose-Hubbard model in Eq. (1) with kinetic frustration due to either the size of the Hilbert space (ED) or the frustration (PEPS, QMC). We use a low-entanglement (mean-field) approach. We do not expect that it can describe a spin-liquid phase. However, the estimates presented here can be used as a starting point to initiate experimental quantum simulations.

This paper is organized as follows. In Section II, we discuss a specific experimental setup to realize the trian-

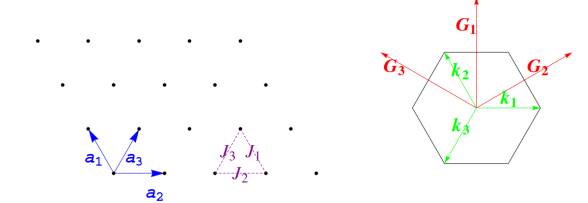


FIG. 1: (Color online.) The triangular lattice in real space (left) and the corresponding reciprocal lattice vectors with the Brillouin zone (right). The experimental setup proposed here has a fixed geometry, and the anisotropy of the hopping rates is realized by different intensities of the laser beams creating the optical lattice potential. Note that in comparison to optical lattices created using standing waves, the lattice spacing is larger, $|\mathbf{a}_i| = 2\lambda_L/3$.

gular lattice and outline the band structure calculation. Section III. is devoted to the discussion of the experimental parameters based on the setup and the corresponding microscopic parameters. We also discuss the procedure of reversing the interaction U and harmonic potential V_0 . In Section IV. we outline the numerical simulation method. The results of the simulations are shown and their implications are discussed in Section V.

II. TRIANGULAR OPTICAL LATTICE

Following Ref. [25], we consider three phase stabilized running waves at blue detuning with some wavelength λ_L in 120° angles. The corresponding electric field is given by

$$\mathbf{E} = \sum_{i=1,2,3} E_i \hat{\epsilon}_i \cos(\mathbf{k}_i \mathbf{r} - \omega_L t), \quad (2)$$

where E_i are the strengths of the electric field in each plane wave, ω_L is the laser frequency, the wave vectors are

$$\mathbf{k}_1 = k_L (1, 0), \mathbf{k}_{2,3} = k_L \left(-\frac{1}{2}, \pm \frac{\sqrt{3}}{2} \right), \quad (3)$$

with the wave number $k_L = 2\pi/\lambda_L$, and the polarizations $\hat{\epsilon}_i$ lie in the plane of propagation,

$$\hat{\epsilon}_i = k_L^{-1} (\hat{z} \times \mathbf{k}_i). \quad (4)$$

The time averaged laser intensity can be reparameterized conveniently as the optical lattice potential

$$V(\mathbf{r}) = V_{\text{offset}} + V_L \sum_{i=1,2,3} (1 + \alpha_i) \sin^2(\mathbf{b}_i \mathbf{r}), \quad (5)$$

where $\mathbf{b}_1 = \frac{1}{2}(\mathbf{k}_2 - \mathbf{k}_3)$, etc., and α_i characterize the anisotropy of the optical lattice potential. For simplicity,

we will consider the case of partial anisotropy $\alpha_1 = -\alpha$ and $\alpha_{2,3} = \alpha/2$ corresponding to $E_1 \geq E_2 = E_3$ [26].

The optical lattice setup discussed above has a fixed lattice geometry. This allows for a direct comparison of the time-of-flight images with different values of α . Rhombic optical lattices can be realized with two standing waves by varying the angle between the beams. However, it is harder to reach the isotropic case (which follows trivially from symmetry with the three-beam setup) and the comparison of TOF images is not so straightforward as the reciprocal lattice vectors change. An additional experimental advantage of the setup proposed here over a two-beam setup is that the laser intensities can be changed more easily than the angle between the beams.

The periodic potential in Eq. (5) defines Bloch bands for a triangular lattice. The lattice vectors $\mathbf{a}_1 = (-1/3, 1/\sqrt{3})\lambda_L$, $\mathbf{a}_2 = (2/3, 0)\lambda_L$, and $\mathbf{a}_3 = \mathbf{a}_1 + \mathbf{a}_2$ are shown in Fig. 1. The band structure parameters for Eq. (1) are calculated using the solution of the two-dimensional one-body problem in the optical lattice potential (5): For each fixed momentum \mathbf{k} of the Brillouin zone (BZ), we calculate the eigenvalues and eigenvectors of the block matrix (note rescaling in terms of the recoil energy $E_R = \hbar^2 k_L^2 / 2M$)

$$h_{\tilde{\mathbf{k}},\tilde{\mathbf{k}'}} = \delta_{\tilde{\mathbf{k}'},\tilde{\mathbf{k}}} \frac{\tilde{k}^2}{k_L^2} - \frac{V_L}{4E_R} \sum_{j=1}^3 (1 + \alpha_j) [\delta_{\tilde{\mathbf{k}'},\tilde{\mathbf{k}}+\mathbf{G}_j} + \delta_{\tilde{\mathbf{k}'},\tilde{\mathbf{k}}-\mathbf{G}_j}] \quad (6)$$

where the extended momentum $\tilde{\mathbf{k}} = \mathbf{k} + g_1 \mathbf{G}_1 + g_2 \mathbf{G}_2$ can be indexed by the integers $g_{1,2} \in [-g_c, g_c - 1]$ and $\mathbf{G}_j = 2\mathbf{b}_j$. The lowest eigenvalues of Eq. (6) as a function of \mathbf{k} define the lowest Bloch band, which is approximately a nearest-neighbor dispersion relation,

$$\epsilon_{\mathbf{k}} = -2 \sum_{j=1,2,3} J_j \cos(\mathbf{k} \cdot \mathbf{a}_j), \quad (7)$$

for the parameter values of V_L and α relevant to this work. Due to the partial potential anisotropy, there is partial hopping anisotropy $J_1 = J_3 > J_2$ for $\alpha > 0$.

The minimum of the non-interacting dispersion relation $\epsilon_{\mathbf{k}}$ is at $\mathbf{k} = 0$ momentum, while the *maxima* lie at

$$\mathbf{k}_{A,B} = \left(\pm k^*, \frac{\sqrt{3}}{2} k_L \right); k^*/k_L = \frac{3}{2\pi} \arccos \left(\frac{J_1}{2J_2} \right). \quad (8)$$

These points coincide with the corners of the Brillouin zone in the isotropic case, $J_1 = J_2 = J_3$ ($\alpha = 0$). The momenta are not equivalent in terms of modulo reciprocal lattice vectors, $\mathbf{k}_A \not\cong \mathbf{k}_B \cong -\mathbf{k}_A$, leading to the possibility of the Z_2 (chirality) symmetry breaking [14, 15]. The vectors $\mathbf{k}_{A,B}$ for a general α are incommensurate with the lattice. The value of k^* decreases for $\alpha > 0$ and vanishes at the rhombic transition point $\alpha = \alpha_c$ when $J_1 = 2J_2$. For stronger anisotropy, the lattice links with the stronger hopping define a rhombic lattice.

TABLE I: Band parameters in the isotropic case ($\alpha = 0$) for different values of the lattice depth V_L . The bandwidth of the lowest band $\epsilon_{\mathbf{k}}$ is W , and Δ gives the gap between the lowest Bloch band and the next one. Next-nearest neighbor hopping can be neglected when $|W - 9J_1| \ll J_1$.

	V_L/E_R	W/E_R	Δ/E_R	J_1/E_R	Δ/W
1.	0.529	0.572	0.0627024	1.08	
2.	0.257	1.412	0.0295701	5.59	
3.	0.116	2.233	0.0133173	19.28	
4.	0.0548	2.975	0.00625151	54.26	
5.5	0.0195	3.903	0.00221681	199.9	

The joint set of elements of all eigenvectors $v_{\tilde{\mathbf{k}}}$ of the lowest band define the *Fourier components* of the Wannier function up to a phase factor,

$$w(\tilde{\mathbf{k}}) \sim v_{\tilde{\mathbf{k}}} \rightarrow w_j(\mathbf{r}) = \sum_{\tilde{\mathbf{k}}} e^{i\tilde{\mathbf{k}}(\mathbf{r}-\mathbf{r}_j)} w_{\tilde{\mathbf{k}}}, \quad (9)$$

which is used on one hand to calculate the envelope for the time-of-flight (TOF) images and to define the dimensionless interaction overlap integral

$$u = k_L^{-2} \int d^2 \mathbf{r} |w_0(\mathbf{r})|^4. \quad (10)$$

III. EXPERIMENTAL AND MODEL PARAMETERS

We consider blue detuned laser beams at wavelength $\lambda_L = 736.65$ nm for ^{39}K atoms, which was used in the experiment described in Ref. [20]. This implies that the recoil energy is

$$E_R = \frac{\hbar^2 k_L^2}{2M} \approx 450 \text{ nK} \approx 9.4 \text{ kHz}. \quad (11)$$

Hopping amplitudes and other band parameters in the isotropic case are shown in Table I and for the anisotropic case in Tables II and III.

The external harmonic potential has a bare strength \bar{V} ,

$$V_0/E_r \equiv \pm \bar{V} \nu^2 \approx \pm 2.78 \times 10^{-8} \nu^2, \quad (12)$$

where the value of the trapping frequency ν is in units of Hz. The upper sign corresponds to the usual trapping potentials, the lower sign is active for the anti-trapping situation.

The on-site interaction is given by [5]

$$U/E_R = 8\pi (a_s k_L) u w_z, \quad (13)$$

where for simplicity, we input the value of the scattering length a_s directly [27]. The interaction overlap $u = u(V_L, \alpha)$ is calculated from the Wannier function in Eq. (10). We consider a layered system similar to

TABLE II: Band parameters for different values of the lattice potential anisotropy α for $V_L = 2E_R$.

α	W/E_R	Δ/E_R	$J_1/E_R = J_3/E_R$	J_2/E_R	Δ/W	J_1/J_2	k^*/k_L	$u(\sim U)$	
0.	0.257	1.412	0.0295701		0.0295701	5.586	1.	0.5	0.167994
0.25	0.262	1.277	0.0320253		0.0254546	4.871	1.25813	0.425	0.167238
0.5	0.275	1.145	0.0347427		0.022295	4.166	1.55832	0.323	0.165063
0.75	0.296	1.01	0.0377333		0.0199259	3.408	1.89368	0.156	0.161633
1.	0.325	0.873	0.0409952		0.0182272	2.689	2.24912	0.	0.157101

TABLE III: Band parameters for different values of the lattice potential anisotropy α for $V_L = 3E_R$. The first column defines the identifiers for the different “protocols”.

α	W/E_R	Δ/E_R	$J_1/E_R = J_3/E_R$	J_2/E_R	Δ/W	J_1/J_2	k^*/k_L	$u(\sim U)$	
a) 0.	0.116	2.233	0.0133173		0.0133173	19.28	1.	0.5	0.226388
b) 0.1	0.118	2.156	0.0139504		0.0121748	18.28	1.14585	0.459	0.226222
c) 0.2	0.121	2.079	0.014631		0.0111764	17.24	1.3091	0.409	0.225722
d) 0.3	0.124	2.003	0.015362		0.0103051	16.16	1.49072	0.348	0.224902
e) 0.4	0.128	1.926	0.0161468		0.0095464	15.08	1.6914	0.269	0.223772
f) 0.5	0.134	1.847	0.0169886		0.008888	13.74	1.91141	0.143	0.222343
g) 0.6	0.142	1.768	0.0178908		0.00831952	12.48	2.15046	0.	0.220625
h) 0.7	0.150	1.689	0.0188569		0.00783222	11.30	2.40761	0.	0.218627

Ref. [21] with a vertical optical lattice depth $V_{L,\text{ver}} = 25E_R$ [28], which corresponds to a vertical hopping $J_z \approx 0.00104E_R$ and Wannier overlap $w_z \approx 0.848035$.

To reach negative absolute temperatures in Ref. [20], the experimental parameters (horizontal and vertical optical lattice intensities, magnetic field, etc.) were changed via an involved protocol. However, most of these steps emerge as a technical necessity. Furthermore, the cloud is initially trapped in a very deep optical lattice where the atom density distribution is essentially frozen. From this perspective, most steps of the experimental protocol are almost instantaneous.

To simplify the numerical simulations and to improve the transparency of the text, we consider an *instantaneous quench* in the system: For time $t < 0$, we take an isotropic ($\alpha_i = 0$) triangular lattice with depth $V_{L,i} = 5.5E_R$, a scattering length $a_{s,i} = +400a_{\text{Bohr}}(U/J_1 \approx 582)$ and $\nu_i = 60$ Hz horizontal trapping frequency ($V_0/E_R \approx 0.0001$) for a strongly compressed Mott insulator initial ground state in equilibrium. At $t = 0$, we instantaneously change to a shallower optical lattice $V_{L,f} < V_{L,i}$, a negative scattering length $a_{s,f} < 0$ and an anti-trapping harmonic potential $V_0,f < 0$ [29].

The optimal final lattice depth for the numerical and the experimental setups depends on various aspects.

Fast enough dynamics certainly requires weak enough $V_{L,f}$. Avoiding technical heating from the blue detuned lattice lasers also favors weaker lattice potentials.

On the other hand, there are more arguments in favor of a relatively deep lattice. If the lattice is too weak, the Bloch gap between the lowest band and the next band may not be large enough [c.f. Tables II and III]. This is unfavorable since the protocol strongly relies on the bounded kinetic energy, which is violated if the tunnel-

ing rate to other Bloch bands is not negligible. In weaker lattices the overlap integral for the interaction is also reduced and therefore larger scattering lengths are needed to compensate. This usually implies getting closer to a Feshbach resonance [20], where many-body losses are enhanced. Last, the value of the lattice potential anisotropy is bounded, $\alpha \leq 1$, since the wave intensities cannot be negative, cf. Eq. (5). Additionally, for $V_L = 3E_R$, the rhombic transition happens at a lower value of α than for $V_L = 2E_R$ (c.f. Tables II and III), which might be favored experimentally.

Taking these considerations into account, we will mainly focus on the parameters $V_{L,f} = 3E_R$, a scattering length $a_{s,f} = -50a_{\text{Bohr}}$, and anti-trapping $\nu_f = 30$ Hz ($V_0/E_R \approx -0.000025$).

IV. TIME-DEPENDENT GUTZWILLER ANSATZ

We apply the time-dependent Gutzwiller ansatz (GA) [21, 30–35] to study the dynamics of the cloud after the quench defined in the previous section. In this approximation, the probability amplitudes of finding precisely m bosons at site j and time t are given by the following set of differential equations:

$$\begin{aligned}
 i\partial_t f_m(j, t) = & [U(t) \frac{m-1}{2} + V_0(t) \mathbf{r}_j^2 - \mu_0] m f_m(j, t) \\
 & - \Phi^*(j, t) \sqrt{m+1} f_{m+1}(j, t) \\
 & - \Phi(j, t) \sqrt{m} f_{m-1}(j, t),
 \end{aligned} \tag{14}$$

where we introduced $\Phi(j, t) = \sum_{\delta} J_{\delta}(t) \langle b_{j+\delta} \rangle$, the index δ running over the nearest neighbor sites and

$$\langle b_j \rangle = \sum_m \sqrt{m+1} f_m^*(j, t) f_{m+1}(j, t). \quad (15)$$

In Ref. [21] we studied a similar setup corresponding to the experiments in Ref. [20] on the square lattice, with four nearest neighbor sites. The isotropic triangular lattice with six nearest neighbors is closer to the mean-field limit than the square lattice, however, frustration is expected to enhance quantum fluctuations which are captured poorly in the mean-field approximation. Similar to Ref. [21], we focus only on a single layer and entirely neglect the hopping between layers.

The lattice consists of 192×192 lattice sites. The initial state is a strongly compressed Mott insulator, which is determined as the ground state of Eq. (1) in the equilibrium variational GA for the initial parameters. The total atom number is $N_{\text{tot}} \approx 2260$. To numerically integrate Eq. (14) we use the fourth-order Runge-Kutta method and the (conserved) total atom number

$$\begin{aligned} N_{\text{tot}} &= \sum_j n_j(t), \text{ with} \\ n_j(t) &= \sum_m m |f_m(j, t)|^2, \end{aligned} \quad (16)$$

serves as a primary measure of numerical accuracy.

V. NUMERICAL RESULTS

We calculate various (macroscopic) quantities as a function of time, as defined in Ref. [21]. The time evolution of the condensate fraction

$$N_0(t) = \sum_j |\langle b_j \rangle|^2, \quad (17)$$

and nearest-neighbor coherences

$$C(\delta, t) = \sum_{j, \delta} \langle b_j^\dagger \rangle \langle b_{j+\delta} \rangle \quad (18)$$

follow a qualitatively similar behavior as on the square lattice [21], C becoming negative, see Fig. 2.

Longer range coherences are calculated in the \mathbf{a}_2 (x-) direction,

$$C(l, t) = \sum_j \langle b_{\mathbf{r}_j}^\dagger \rangle \langle b_{\mathbf{r}_j+l\mathbf{a}_2} \rangle, \quad (19)$$

$$\tilde{C}(l, t) = \sum_j \frac{\langle b_{\mathbf{r}_j}^\dagger \rangle}{\sqrt{n(\mathbf{r}_j)}} \frac{\langle b_{\mathbf{r}_j+l\mathbf{a}_2} \rangle}{\sqrt{n(\mathbf{r}_j+l\mathbf{a}_2)}}, \quad (20)$$

the latter being normalized so that it is less sensitive to spatial inhomogeneities.

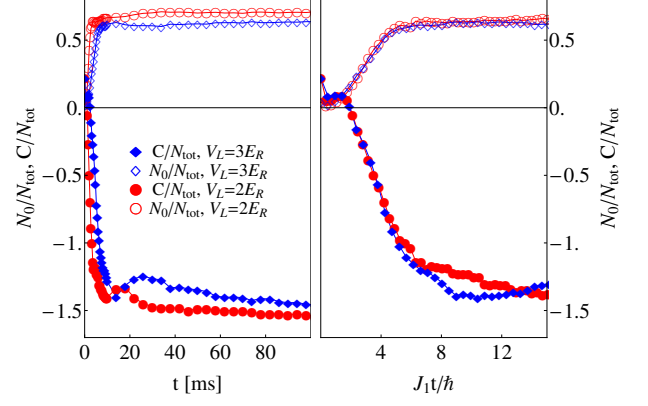


FIG. 2: (Color online.) Left: Condensate fraction $N_0(t)$ and nearest-neighbor coherences $C(t)$ as a function of time t in the isotropic case $\alpha = 0$. Right: the same quantities with the time axis rescaled to $J_1 t / \hbar$, showing a collapse of the initial dynamics.

We calculate two-dimensional TOF images using the formula (following Ref. [5])

$$I_{\text{TOF}}(\tilde{\mathbf{k}}) = |w(\tilde{\mathbf{k}})|^2 \mathcal{G}(\tilde{\mathbf{k}}) \quad (21)$$

where the envelope $|w(\tilde{\mathbf{k}})|^2$ is the Fourier transform of the Wannier function (c.f. Eq. (9)) and the Fourier transform of the single-particle density matrix is given in the GA by

$$\mathcal{G}(\mathbf{k}) = |\langle b_{\mathbf{k}} \rangle|^2 + (N_{\text{tot}} - N_0), \langle b_{\mathbf{k}} \rangle = \sum_j e^{i\mathbf{k}\mathbf{r}_j} \langle b_j \rangle. \quad (22)$$

This normalization implies $\sum_{\mathbf{k} \in BZ} \mathcal{G}(\mathbf{k}) = N_{\text{tot}}$, and makes direct comparisons of the absolute TOF intensities possible.

A. Numerical results for the isotropic lattice

We compare macroscopic quantities for two different sets of the final parameters, $V_{L,f} = 2E_R, a_{s,f} = -100a_{\text{Bohr}}$ and $V_{L,f} = 3E_R, a_{s,f} = -50a_{\text{Bohr}}$ in Fig. 2. The interaction strengths are $U/J_1 \approx -5.5$ and $U/J_1 \approx -8.2$, respectively. TOF images at $t = 200$ ms are shown for comparisons in Fig. 3.

Since in the case of the deeper lattice $V_{L,f} = 3E_R$ the system is closer to the hard-core limit and yet the corresponding TOF images show more enhanced peaks with a pronounced chirality, we will consider this lattice depth in the following.

B. Numerical results for the anisotropic lattice

In this subsection we display macroscopic quantities and TOF images for different values of the potential

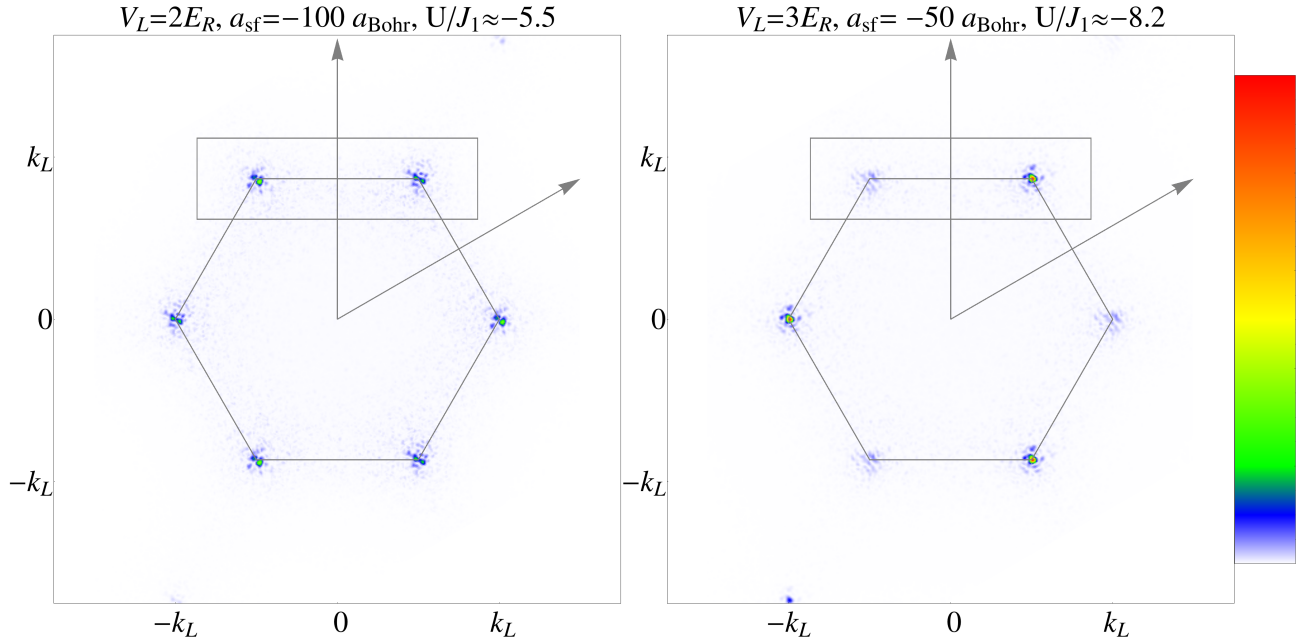


FIG. 3: (Color online.) TOF images at $t = 200$ ms for a weaker ($V_L/E_R = 2$, $U/J_1 \approx -5.5$) and a stronger final lattice ($V_L/E_R = 3$, $U/J_1 \approx -8.2$) in the isotropic case. Note that the latter image shows a strong chirality. The arrows represent the reciprocal lattice vectors \mathbf{G}_1 and \mathbf{G}_2 , the hexagon represents the border of the first BZ. The rectangular area is displayed in Fig. 6.

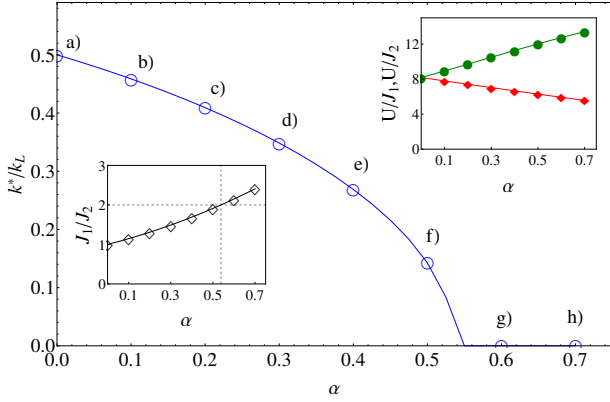


FIG. 4: (Color online.) The value of k^* as defined by Eq. (8) as a function of the optical potential anisotropy α for $V_L = 3E_R$. Insets: Microscopic parameters for the different values of α listed in Table III. The rhombic transition point corresponds to $\alpha = \alpha_c \approx 0.55$.

anisotropy α for the final lattice depth $V_{L,f} = 3E_R$. The microscopic parameters are listed in Table III and shown in Fig. 4.

The condensate fractions N_0 , the nearest-neighbor coherences C and the total double occupation D_{tot} is shown in Fig. 5 as a function of time t for the different values of α .

We show the relevant part of the TOF images for the different values of α in Fig. 6. For weak anisotropies $\alpha \leq 0.4$, we observe coherence manifesting in peaks at

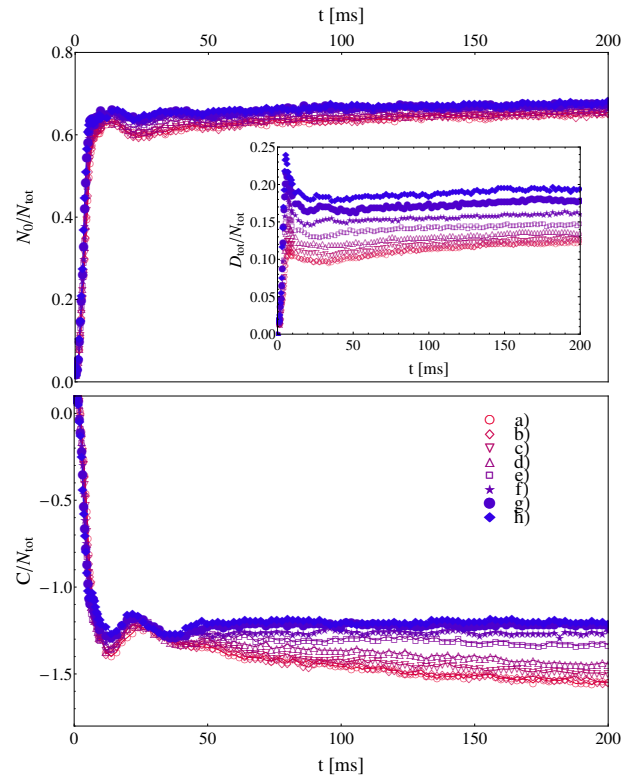


FIG. 5: (Color online.) Macroscopic parameters as a function of time t for the different values of α listed in Table III. Note that the condensate fraction N_0 varies very weakly with α .

the corresponding quasi-classical maxima \mathbf{k}_A or \mathbf{k}_B of the free dispersion. Beyond the rhombic transition point, $2J_2 < J_1$ or $\alpha > 0.55$, there is also apparently coherence at the “Neel” momentum $\mathbf{Q} = (0, \sqrt{3}/2)k_L$. However, for the intermediate value $\alpha = 0.5$ (case f), there are no peaks at the quasi-classical maxima, furthermore, no dominant coherent peak is found up to $t = 600$ ms of the numerical simulation.

To complement the TOF images, we calculated longer ranged coherences, shown in Fig. 7. While the density normalized coherences \tilde{C} are more noisy, they follow qualitatively the course of the corresponding unnormalized coherences, which in turn is well approximated in most cases by

$$C(x) \approx c(x)e^{i\kappa x}, \kappa = k^* + i\xi^{-1}, \quad (23)$$

and $c(x)$ varies weakly. The notable exception is the case f), without any apparent oscillating component and a coherence length ξ of the order of one lattice spacing. From Eq. (23) it is obvious that coherence cannot be defined if the condition for coherent behavior

$$k^*\xi \gg 1 \quad (24)$$

breaks down, i.e., when the “pitch length” of the spiral in the x-direction, $\sim 1/k^*$, becomes longer than the coherence length ξ . Since $k^* = k^*(\alpha) \sim \sqrt{\alpha_c - \alpha} \rightarrow 0$ at the rhombic transition, it is important how ξ depends on the various parameters and system size around $\alpha \approx \alpha_c$. Unfortunately, this question cannot be addressed properly using the present approach.

An obvious reason for the lack of coherence could be an anomalously long “relaxation” time due to the various approximations, and the experimental system (or even the “true” dynamics under Eq. (1)) could display coherence in shorter times. However, this claim is only partially justified. It is true that within the time-dependent GA defined by Eq. (14) the “relaxation” is slow as it is driven by *dephasing*, i.e., by the mismatch between local mean-field Hamiltonians. The true dynamics governed by Eq. (1) should lead to a faster *equilibration* in general. However, the main candidate state for stronger on-site interactions has simply Neel-type coherence [10, 36], which is found to develop for $J_1 > 2J_2$. Therefore it is quite puzzling why GA fails to find such a mean-field type solution.

Regarding time scales, one should also not forget about *losses and decoherence* in the experimental system, which includes all processes that are left out from Eq. (1): technical heating from the lasers, multiband contributions, many-body losses driven by three-body recombination, etc. These determine the experimental lifetime and provide an upper bound to the coherence lifetime. For the optimal square-lattice setup it was found to be on the order of 700 ms [20].

VI. CONCLUSIONS

We proposed a specific experimental setup for interacting bosons on an anisotropic triangular lattice and cal-

culated the microscopic parameters for the corresponding Bose-Hubbard model. We studied numerically the dynamics of the atoms in a time-dependent mean-field approximation after instantaneously reversing the signs of the on-site interaction to $U_f < 0$ and the external potential to $V_{0,f} < 0$. We found that quasi-classical coherence with 120° spiral order develops in the isotropic case. This can be interpreted as a manifestation of the “frustrated” kinetic term of the Bose-Hubbard model at a negative absolute temperature. We also found the expected Neel-type antiferromagnetic ordering in the rhombic limit. Curiously, for a certain value of the anisotropy, no (quasi-classical) coherence is found up to 600 milliseconds after the quench. We were not able to rule out whether this is an artifact of the approximations. It is not possible to compare these results to unbiased numerical methods like QMC or PEPS, since the description of homogeneous equilibrium states are already quite challenging.

Based on the qualitative agreement between experiments [20] and the numerical simulations in the time-dependent Gutzwiller approximation [21] for the square lattice, we believe that the coherence observed here both in the isotropic and in the rhombic limit implies that the relevant experimental parameter regime can be accessed by the “negative-T” approach also for the triangular lattice. This allows for an experimental investigation of unconventional superfluidity and potentially also to reach the conjectured spin liquid behavior of the quantum XY-model [10, 13].

We did not study the chirality of the spiral order in detail as in a layered setup with independent layers and TOF images taken vertically, this feature cannot be accessed easily.

An interesting future direction would be the generalization of the Feynman relation [37] to unconventional superfluids on the triangular lattice. This relation gives a variational estimation of the dispersion relation of the low-energy excitations $E_{\mathbf{q}}$ as a ratio of the non-interacting kinetic energy $\epsilon_{\mathbf{k}}$ and the form factor $S(\mathbf{q})$ (Fourier transform of the density-density correlation function). In particular, Feynman was capable to reproduce approximately the phonon-roton spectrum for superfluid He using the form factor measured by neutron scattering. For ultracold atoms, the form factor could be extracted from noise correlations of TOF images [5, 38], which could be used to reveal the low-energy dispersion relation of the excitations, in particular, the dynamical exponent z from the relation $E_{\mathbf{q}} \sim q^z$ at low momenta.

Acknowledgements. I am grateful for discussions with Hendrik Weimer, Ricardo Doretto, Temo Vekua, Luis Santos, and Ulrich Schneider. I thank especially Stephan Mandt for a critical reading of the manuscript. This research was financially supported by the DFG.

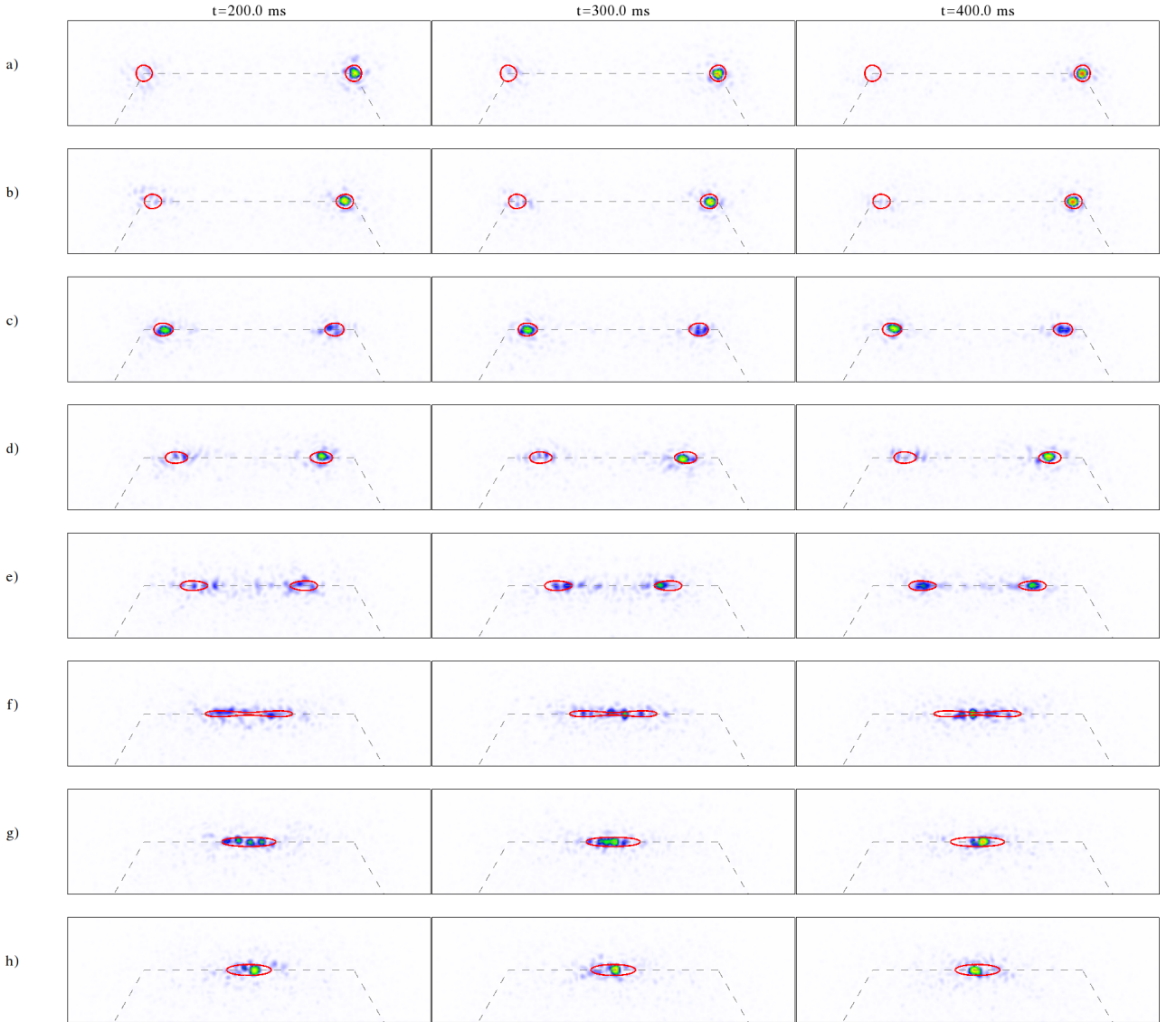


FIG. 6: (Color online.) Parts of the TOF images at $V_{L,f} = 3E_R$ for different values of α . The rows a) - h) correspond to different values of the lattice potential anisotropy α (c.f. Table III and Fig. 4), the columns correspond to different times after the quench. The color coding is similar to Fig. 3. The gray dashed line corresponds to the border of the BZ. The red contours are defined to enclose 128 points with the highest kinetic energy ϵ_k in reciprocal space for the lattice size of 192×192 .

[1] G. H. Wannier, Phys. Rev. **79**, 357 (1950).
 [2] D. J. P. Morris, D. A. Tennant, S. A. Grigera, B. Klemke, C. Castelnovo, R. Moessner, C. Czter-nasty, M. Meissner, K. C. Rule, J.-U. Hoffmann, K. Kiefer, S. Gerischer, D. Slobinsky, and R. S. Perry Science **326**, 411 (2009).
 [3] P. A. M. Dirac, Proc. Roy. Soc. (London) A **133**, 60 (1931).
 [4] L. Balents, Nature **464**, 199 (2010).
 [5] I. Bloch, J. Dalibard, and W. Zwerger, Rev. Mod. Phys. **80**, 885 (2008).
 [6] T. Müller, S. Fölling, A. Widera, and I. Bloch, Phys. Rev. Lett. **99**, 200405 (2007).
 [7] M. Ölschläger, G. Wirth, and A. Hemmerich, Phys. Rev. Lett. **106**, 015302 (2011).
 [8] A. Koetsier, R. A. Duine, I. Bloch, and H. T. C. Stoof, Phys. Rev. A **77**, 023623 (2008).
 [9] A. Eckardt, C. Weiss, and M. Holthaus, Phys. Rev. Lett. **95**, 260404 (2005).
 [10] A. Eckardt *et al.*, EPL **89**, 10010 (2010).
 [11] S. Miyashita and H. Shiba, Phys. Soc. Jpn. **53**, 1145 (1984).
 [12] R. Schmied, T. Roscilde, V. Murg, D. Porras, and J. I. Cirac, New J. Phys. **10** 045017, (2008).
 [13] P. Hauke, Phys. Rev. B **87**, 014415 (2013).
 [14] J. Struck, C. Ölschläger, R. Le Targat, P. Soltan-Panahi, A. Eckardt, M. Lewenstein, P. Windpassinger, and K.

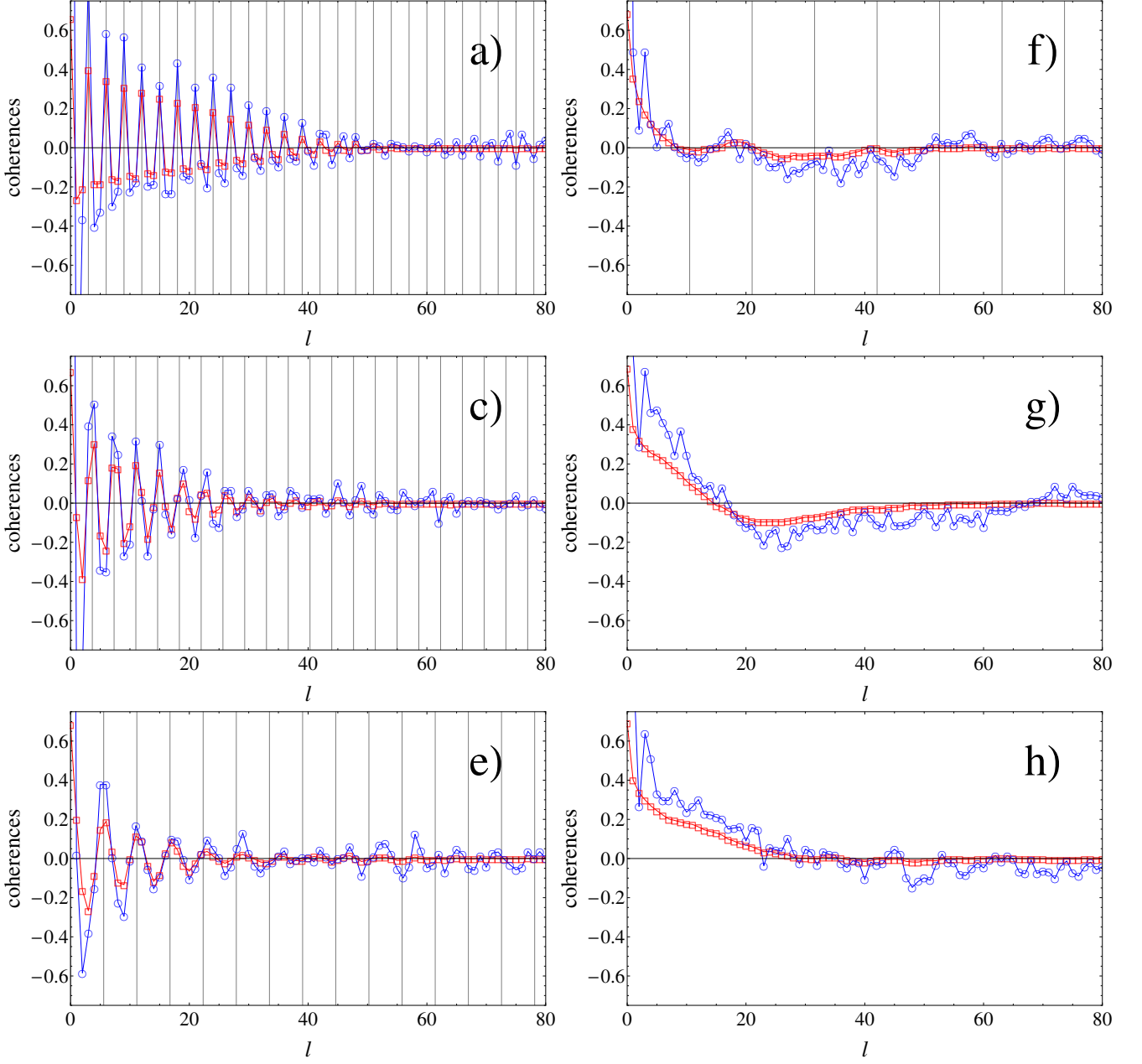


FIG. 7: (Color online.) Longer-range coherences in the \mathbf{a}_2 (x-) direction as a function of the site index l at time $t = 400$ ms. Red squares: $\text{Re } C(l)$, blue circles: $\text{Re } \tilde{C}(l)$. The grid lines represent the quasi-classical “pitch” length $2\pi/|\mathbf{a}_2|k^*$ of the spiral ordering vector.

Sengstock, Science **333**, 996 (2011).

- [15] J. Struck, M. Weinberg, C. Ölschläger, P. Windpassinger, J. Simonet, K. Sengstock, R. Höppner, P. Hauke, A. Eckardt, M. Lewenstein, and L. Mathey, Nature Physics **9**, 738 (2013).
- [16] L. D. Landau and E. M. Lifshitz, *Statistical Physics Part 1* (Pergamon, New York, 1980), 3rd ed.
- [17] A. P. Mosk, Phys. Rev. Lett. **95**, 040403 (2005).
- [18] Á. Rapp, S. Mandt, and A. Rosch, Phys. Rev. Lett. **105**, 220405 (2010).
- [19] Á. Rapp, Phys. Rev. A **85**, 043612 (2012).
- [20] S. Braun, J. P. Ronzheimer, M. Schreiber, S. S. Hodgman, T. Rom, I. Bloch, and U. Schneider, Science **339**, 52 (2013).
- [21] Á. Rapp, Phys. Rev. A **87**, 043611 (2013).
- [22] S. Mandt, A. E. Feiguin, S. R. Manmana, Phys. Rev. A **88**, 043643 (2013).
- [23] F. Verstraete and J. I. Cirac, preprint, cond-mat/0407066 (2004).
- [24] L. Pollet, K. Van Houcke, S. M. A. Rombouts, J. of Comp. Phys. **225**, 2249 (2007).
- [25] C. Becker *et al.*, New J. Phys. **12**, 065025 (2010).
- [26] Deploying full anisotropy in experiments should not

present a problem.

- [27] The values of the scattering length a_s used here for ${}^{40}\text{K}$ can be inverted for the magnetic field value B using the parameters of the corresponding Feshbach resonance.
- [28] The vertical standing wave should be detuned by a few MHz from the horizontal running beams.
- [29] Experimentally, the negative scattering length can be achieved by ramping the magnetic field through a Feshbach resonance. The anti-trapping potential is provided mainly by the beam profile of the blue-detuned vertical optical lattice beams.
- [30] D. Jaksch, V. Venturi, J. I. Cirac, C. J. Williams, and P. Zoller, Phys. Rev. Lett. **89**, 040402 (2002).
- [31] J. Zakrzewski, Phys. Rev. A **71**, 043601 (2005).
- [32] M. Snoek, EPL **95**, 30006 (2011).
- [33] S. S. Natu, K. R. A. Hazzard, and E. J. Mueller, Phys. Rev. Lett. **106**, 125301 (2011).
- [34] M. Jreissaty, J. Carrasquilla, F. A. Wolf, and M. Rigol, Phys. Rev. A **84**, 043610 (2011).
- [35] J.-S. Bernier, D. Poletti, P. Barmettler, G. Roux, and C. Kollath, Phys. Rev. A **85**, 033641 (2012).
- [36] P. Hauke, T. Roscilde, V. Murg, J. I. Cirac, and R. Schmied, New J. of Physics, **12**, 053036 (2010).
- [37] R. P. Feynman: *Statistical Mechanics* (ABC ppbk, ISBN 0-201-36076-4).
- [38] E. Altman, E. Demler, and M. D. Lukin, Phys. Rev. A **70**, 013603 (2004).